Biointerface Research in Applied Chemistry
Open-Access Journal (ISSN: 2069-5837)

Article
Volume 13, Issue 4, 2023, 395
https://doi.org/10.33263/BRIAC134.395

Microstructure and Elastic Properties of Hydroxyapatite/Alumina Nanocomposites Prepared by Mechanical Alloying Technique for Biomedical Applications

Rasha A. Youness [1,*], Hisham A. Saleh [2], Mohammed A. Taha [3]

[1] Spectroscopy Department, National Research Centre, El Buhouth St., 12622 Dokki, Giza, Egypt; rhakamnrc@gmail.com (R.A.Y.);
[2] Electron Microscope and Thin Films Department, Physics Research Institute, National Research Centre, At., Doll Giza 12622, Egypt; hishamsalehnrc@yahoo.com (H.A.S.);
[3] Solid State Physics Department, National Research Centre, El Buhouth St., 12622 Dokki, Giza, Egypt; mtahanrc@gmail.com (M.A.T.);
* Correspondence: rhakamnrc@gmail.com (R.A.Y.);

Received: 13.06.2022; Accepted: 20.07.2022; Published: 1.11.2022

Abstract: Although hydroxyapatite (HA) has exceptional biological qualities that inspire researchers to employ it as an appealing biomaterial for various purposes, its usage in hard tissue replacement applications is severely restricted because of its fragility. In order to create nanocomposites with the necessary mechanical properties for biomedical applications, HA was produced, and various amounts of alumina (Al_2O_3) were added to it. Additionally, the phase composition of the powdered nanocomposites was examined using the X-ray diffraction (XRD) technique. Crystal sizes, lattice strain, and dislocation density were all estimated as well. In order to measure the produced nanocomposite powders' physical and elastic characteristics using the Archimedes method and ultrasonic non-destructive technique, they were then pressed and sintered at 1000 °C. The resulting information made it clear that further increases in the weight percentages of Al_2O_3 resulted in a 10.25, 25.64, and 33.33% reduction in crystal size. As a result of adding more Al_2O_3-up to 20 weight, percent-the results also showed that this properties-microhardness, compressive strength, Young's modulus, elastic modulus, bulk modulus, shear modulus, and Poisson's ratio-were improved by 109, 36.29, 95.5, 100.59, 104.97, 92.84 and 9.5%, respectively. Unfortunately, it increased its porosity by considerable amounts. It might be argued that the generated nanocomposites are favorable for biomedical applications.

Keywords: Hydroxyapatite; Nanobiocomposites; Alumina; Microstructure; Physical properties; Mechanical performance.

1. Introduction

Due to the extensive range of biomaterials' uses in biomedicine, ongoing biomaterials research and development is in great demand today. Importantly, a number of parameters, including adequate mechanical qualities, optimal porosity, outstanding bioactivity, and biocompatibility, influence the selection of the ideal biomaterials [1,2]. They must also have a variety of morphologies and forms in order to be used in various biological applications. Monolithic materials, however, cannot satisfy these criteria. Therefore, creating a multiphase material, often known as "composite", that may closely mimic genuine bone is an appealing method to address these pressing needs. Notably, several industrial industrial and biomedical applications

need composite materials [3-8]. Importantly, these composites' better physical and mechanical characteristics result from their synthesis in the nanoscale range [9,10]. Notably, the mechanical alloying (MA) technique makes it simple to produce such desirable composites [11-14]. In order to create appealing biomaterials for various purposes, several biocomposites have been produced in our recent work with a thorough examination of their varied features [15-21].

Due to its exceptional qualities compared to other biomaterials, hydroxyapatite (HA) is frequently employed in orthopedic and dental applications [22]. Since carbonate $(CO_3)^{2-}$ groups can partially replace hydroxyl and phosphate sites that produce A-type or B-type carbonated hydroxyapatite (CHA), it is also hypothesized that adding these groups to the crystal structure of HA will improve its solubility and biological performance. Additionally, it should be mentioned that CHA production in the nanoscale range results in improved characteristics [23,24]. Due to its low mechanical qualities, its clinical uses are sadly limited to non-load–bearing areas [25,26]. To solve this major issue, it is thus imperative to enhance its mechanical characteristics by reinforcing it with a different phase with the necessary mechanical strength [27-30].

Nearly inert bioceramic, i.e., alumina (Al_2O_3), has several desirable properties, including superior corrosion resistance, biocompatibility, and affordability. As a result, it has long been extensively utilized in several biomedical applications [31-33]. When transplanted into the human body, it is unable to connect to live tissues because it lacks bioactivity behavior [14,34]. In order to address this issue, scientists created composites that included Al_2O_3 and a different physiologically active phase.

This study looked at how carbonated hydroxyapatite's physical and mechanical characteristics were affected by adding various weight percentages of alumina.

2. Materials and Methods

2.1. Preparation of CHA nanopowders

In accordance with our most recent research [35,36], calcium carbonate ($CaCO_3$) and calcium hydrogen phosphate dihydrate ($CaHPO_4.2H_2O$) have been used as raw materials to create CHA nanopowders utilizing high-energy ball mill. It is essential to remember that CHA is created using the following eqn.:

$$4CaCO_3+6CaHPO_4.2H_2O \quad Ca_{10}(PO_4)_6(OH)_2+4CO_2+14H_2O \qquad (1)$$

2.2. Preparation of CHA/Al_2O_3 nanopowders.

α-Al_2O_3 powders with 99.99% purity rating and an average particle size of 200 nm), were purchased. Based on their respective weight percentages, the Al_2O_3 and CHA powders were mechanically blended for 10 hours at a speed of 150 rpm with a ball-to-powder ratio (BPR) of 2:1 and 10 mm-diameter balls. These mixtures were then ground for 20 hours in a planetary ball mill with a BPR of 15:1 and a rotational speed of 450 rpm. The milling process was carried out at 5-hour intervals with a 2-hour pause to prevet overheating. Transmission electron microscopy combined with selected area electron diffraction (TEM-SAED); JEOL JEM- 2100 Japan, operated at an accelerating voltage of 120 kV, was used to analyze the morphology and particle size of nanocomposite powders. Table 1 lists the compositions of the powdered nanocomposites that have been created, along with their acronyms.

Table 1. A scheme of the produced specimens with the specimen code and its % composition is shown.

Specimen code	Carbonated hydroxyapatite (CHA)	Alumina (Al_2O_3)
S1	95	5
S2	90	10
S3	85	15
S4	80	20

2.3. Characterization using X-ray diffraction (XRD) technique.

By X-ray diffraction (XRD; Philips PW 1373) device, the structure of the prepared CHA/Al_2O_3 nanocomposites was examined. According to the following equations, the broadening (B) that emerged at 2θ= 32.19 and 33.43° belonging to the diffraction planes (1 1 2) and (3 0 0), respectively, was used to compute the crystallite size (D), lattice strain (ε), and dislocation density (δ) of the produced nanocomposites [37,38]:

$$D = \frac{0.9\,\lambda}{B cos\theta} \quad (2)$$

$$\varepsilon = \frac{B}{4tan\theta} \quad (3)$$

$$\delta = \frac{1}{D2} \quad (4)$$

where: λ= 1.54059°A (Cu-Ni radiation), B is the full width at half maximum (FWHM), and θ is the angle in radians.

2.4. Physical properties of the sintered nanocomposites

As we previously described in our study [23], the milled powders were consolidated into pellets with dimensions of 16 mm in diameter and 4 mm in length using a hydraulic press operating at 50 MPa. Then, using Archimedes' method, bulk density, and apparent porosity were all measured (ASTM: B962-13).

2.5. Mechanical properties.

Vickers microhardness (Hv) was evaluated using a Shimadzu-HMV (Japan) microhardness tester with a 100 g load under ambient laboratory conditions with a constant indenter dwell period of 15 s, as reported in our recent papers [39-43]. Each specimen had at least five indentations measured for each data point. A square-based pyramidal diamond with a face angle of 136 was used to make the indentation, along with a measuring microscope and video monitor:

$$Hv = 1.854\,\frac{P}{D2} \quad (5)$$

where, P is the applied indentation load and D is the measured indentation diagonal.

Microhardness was calculated according to ASTM: B933-09, while the compressive strength was measured according to ASTM E9.

Using the pulse-echo technique with a MATEC Model MBS8000 DSP (ultrasonic digital signal processing) system with a 5 MHz resonating frequency. The ultrasonic wave velocities (longitudinal and shear) propagated in the samples were measured at room temperature. Following are the values of the longitudinal (V^2_L) and shear (V^2_S) ultrasonic velocities that were used to calculate Lame's constants, i.e., λ and μ:

$$\lambda = \rho(V_L^2 - 2V_S^2) \quad (6)$$

$$\mu = \rho V_S^2 \quad (7)$$

$$L = \lambda + 2\mu \quad (8)$$

$$G = \mu \quad (9)$$

$$E = \mu\frac{3\lambda + 2\mu}{\lambda + \mu} \quad (10)$$

$$B = \lambda + \frac{2}{3}\mu \quad (11)$$

$$\upsilon = \frac{\lambda}{2(\lambda + \mu)} \quad (12)$$

where, ρ is the material bulk density, longitudinal modulus (L), shear modulus (G), Young's modulus (E), bulk modulus (B), and Poisson's ratio (υ).

3. Results and Discussion

3.1. Characterization of the prepared nanocomposites powders by TEM-SAED

In this study, TEM-SAED was utilized to examine the diffraction patterns and particle sizes of the raw materials, i.e., HA and Al_2O_3, that were used to create HA/Al_2O_3 composites, as shown in Figure 1 (a,b). Since both materials are depicted in the figure as being in the nanoscale range, there is a strong indication that the required nanocomposites are likewise in this range. In addition to the particle sizes of the materials under investigation, SAED patterns revealed the presence of polycrystalline diffraction rings, which were identified using d-spacing ICCD file cards, as will be explained in the next section. Since nanostructured biomaterials can establish enhanced interactions with proteins and bone-forming cells, this discovery is crucial for biomedical applications [18].

3.2. XRD analysis

The primary method for analyzing the structure of the produced nanocomposite samples was XRD analysis. Therefore, Figure 2 shows the XRD patterns for all manufactured samples. In terms of the positions of the lines at 2θ=32.19, 33.43, 25.74, and 34.19° which correspond to (1 1 2), (3 0 0), (0 0 2), and (2 1 0), respectively, it is important to note from this figure that the distinctive peaks of CHA are well matching with ICPDS card no. 19-0272.

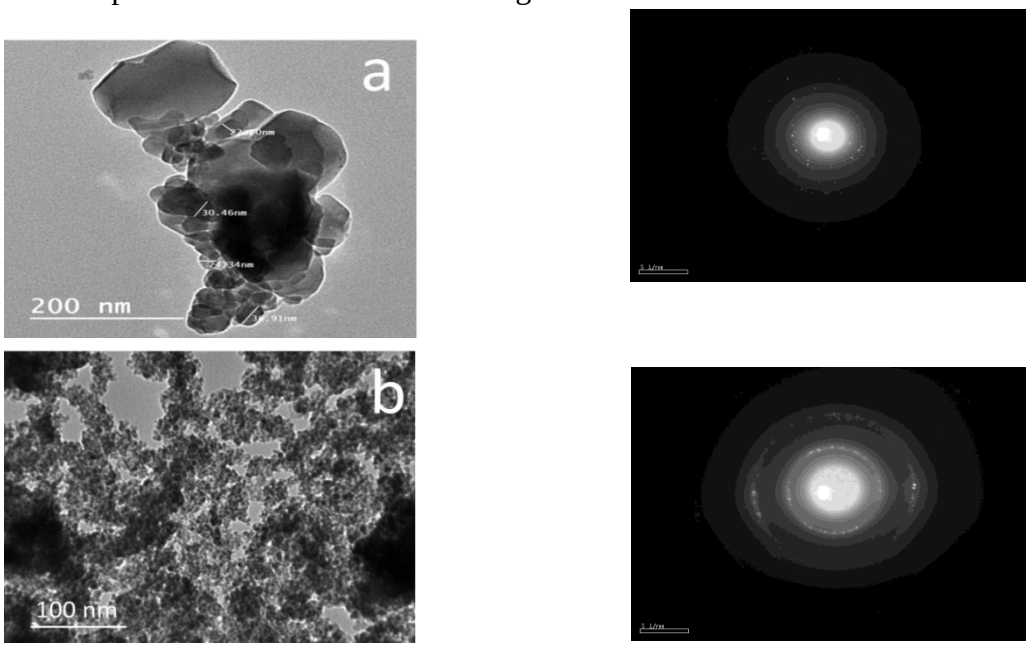

(**a**) (**b**)

Figure 1. TEM images and corresponding SAED patterns of (**a**) HA; (**b**) Al_2O_3 nanopowders.

However, the locations of the Al_2O_3 peaks at 2θ= 35.13, 43.33, 57.47, and 25.56°, which correspond to (1 0 4), (1 1 3), (1 1 6) and (0 1 2), respectively, are in good agreement

with JCPDS card no. 88-0826. Considering that the peaks of Al_2O_3 are less strong and progressively rise with increasing Al_2O_3 levels, it is also feasible to notice that the characteristic peaks of CHA are visible. It is significant to notice that the absence of additional phases demonstrates the purity of the generated nanocomposites.

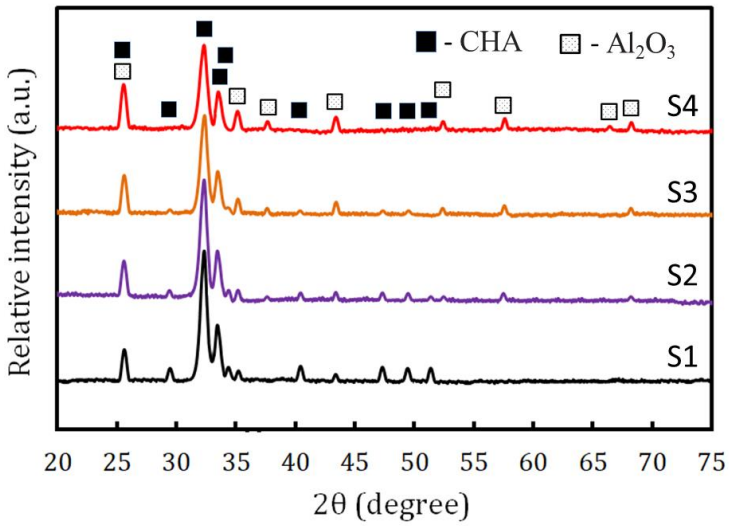

Figure 2. XRD patterns of CHA-based nanocomposite powders with different Al_2O_3 contents (wt.%).

Broadening analysis was used to determine the crystal size, lattice strain, and strain dislocation density since it was anticipated that adding Al2O3 with various contents would impact the microstructure of CHA nanopowders. The results are depicted in figures (3 and 4). On the opposite side, as Al_2O_3 content rises, and lattice strain exhibit the reverse pattern for crystallite sizes. The result is explained by the fact that the presence of Al_2O_3 during the milling process plays a significant role in the occurrence of severe lattice distortion, as well as severe lattice distortion and refinement of grain size, which in turn results in an observed broadness and decreases in the intensities of XRD peaks [42]. It is noteworthy that after 20 hours of milling, the predicted crystal sizes of all examined specimens are 19.5, 17.5, 14.5, and 13 nm. On the other hand, the dislocation density of the same samples is 0.64, 0.70, 0.84, and 0.94%. These findings are quite consistent with those seen in the literature [43-47].

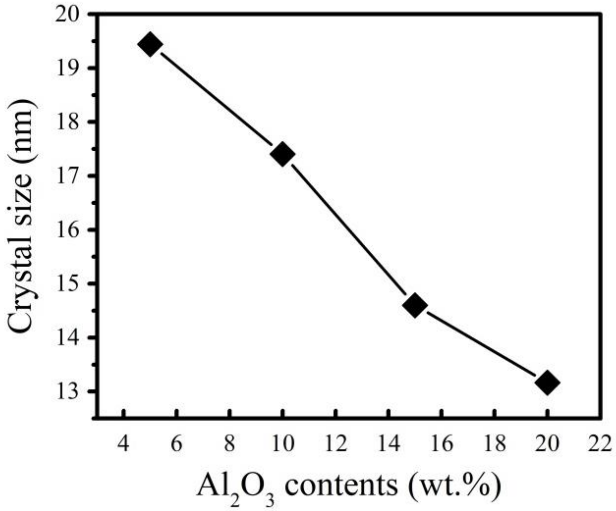

Figure 3. Crystals sizes of CHA/Al_2O_3 nanocomposites powders versus Al_2O_3 contents (wt.%).

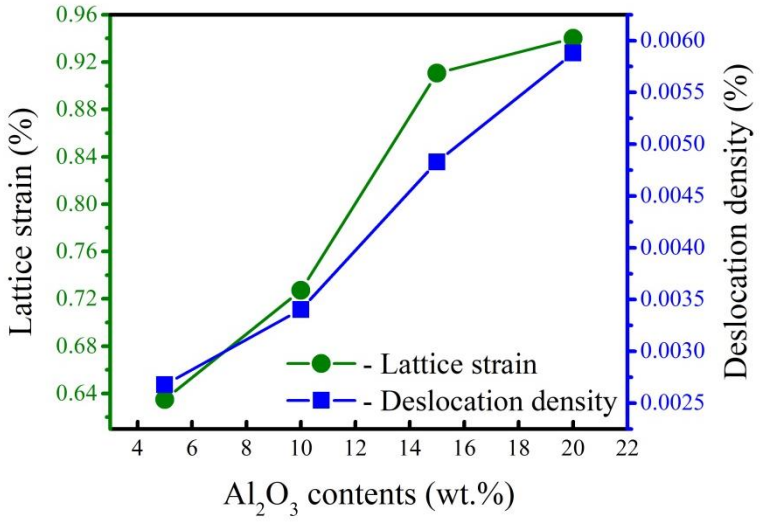

Figure 4. Dislocation density and lattice strain of CHA/Al_2O_3 nanocomposites powders versus Al_2O_3 contents (wt.%).

3.3. Physical properties of the sintered nanocomposites

It is well known that the density values of nanocomposites greatly depend on the porosity of the majority of samples as well as the development of crystalline particles [48]. In order to depict the bulk density and apparent porosity of all sintered samples at 900 °C, Figure 5 was created. It is clear from this graph that the continuous increases in Al_2O_3 contents have resulted in a noticeably higher bulk density. The major discrepancy between the bulk density of Al_2O_3 (3.95 g/cm^3) and the density of HA (3.18 g/cm^3) is responsible for this outcome. Also, because Al2O3 has a much higher porosity than HA, its inclusion in sintered nanocomposites significantly enhances their porosity [49]. It is important to note that the sintering procedure was conducted at this particular temperature to prevent the potential degradation of CHA particles due to their exposure to high temperature, which would cause the formation of tricalcium phosphate and calcium aluminate, which would adversely affect the physical and mechanical properties of the resulting nanocomposites [50,51].

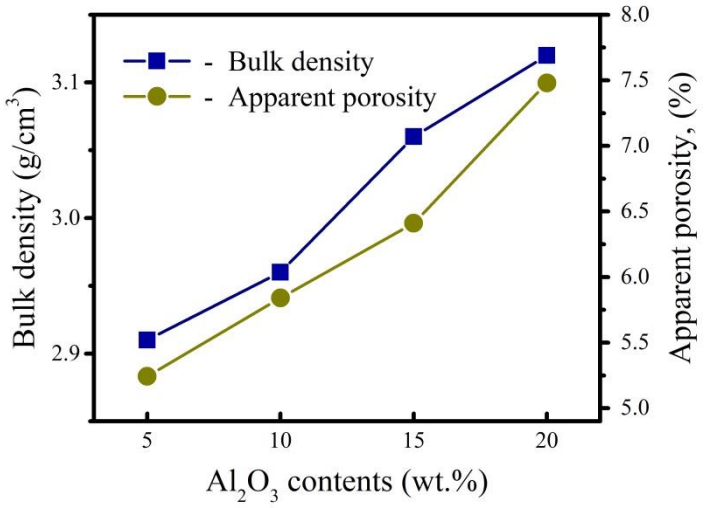

Figure 5. Bulk density and apparent porosity of the sintered samples.

The right sintering temperature is regarded as a crucial element for achieving optimal densification behavior for sintered nanocomposites, as stated in Ref. [52]. There were three phases to the sintering process. The produced particles are first compacted to enable contact

while considering that solid bonding has not yet been accomplished. But as the temperature reaches 2/3 of the melting point, "necks" develop between the particles, resulting in a solid link. As a result, these compacts become denser as the overall emptiness shrinks. Notably, the presence of particles with a large surface area and high surface free energy is what drives the sintering process. When all the particles have bonded together, they can no longer be viewed separately. Importantly, pores are sealed up. Therefore, the remaining porosity has no impact on the mechanical characteristics of the sintered samples. It should be emphasized that while porosity has a detrimental impact on mechanical qualities, it is thought to improve a number of biological aspects. This enhancement is because porosity makes it easier for physiological fluids to enter the samples, which improves the bioactivity behavior. Based on these facts, it is necessary to have a good link between porosity and mechanical qualities to achieve significant applications in bone regeneration [53].

3.4. Mechanical properties

It has been demonstrated that a key aspect of sintered nanocomposites' therapeutic use is their mechanical responsiveness. Accordingly, assessing the mechanical characteristics of all sintered specimens is another focus of this effort. As a result, Figures 6 and 7 show, respectively, microhardness (Hv) and compressive strength.

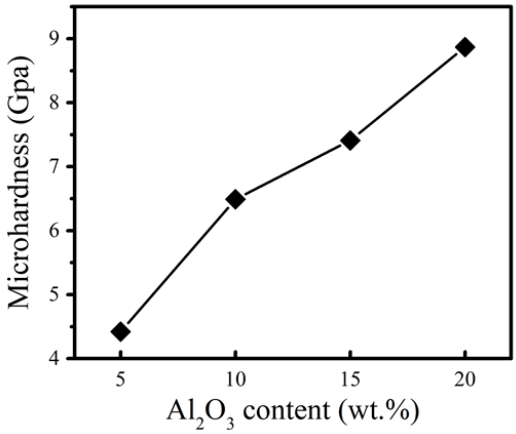

Figure 6. Microhardness of the sintered CHA/Al_2O_3 nanocomposites.

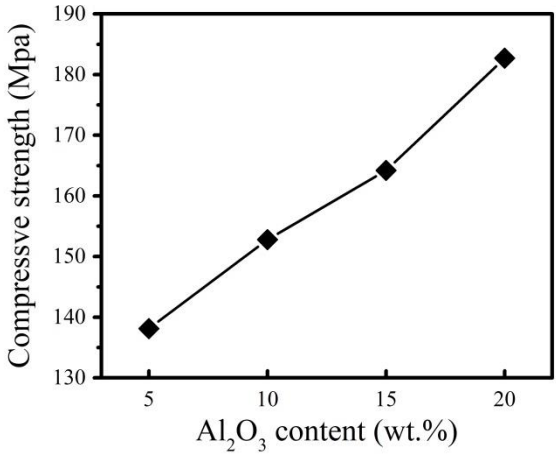

Figure 7. Compressive strength of the sintered CHA/Al_2O_3 nanocomposites.

On the other hand, Table 2 lists the other moduli, such as longitudinal (L), bulk (B), and shear (G). Figure 8 represents Young's modulus (E) and Poisson's ratio (ν), typical of the entire elastic moduli. The results showed that the S4 sample, which has the greatest level of

Al_2O_3, or 20 weight percent, exhibits the poorest due to its low content of Al_2O_3, or 5 weight percent. In the case of the S1 sample, the recorded values are 4.3 GPa, 135 MPa, 41.2 GPa, 46.877 GPa, 29.95 GPa, 16.92 GPa, and 0.21, respectively, whereas, for the S4 sample, they are 9 GPa, 184 MPa, 80.55 GPa, 94.02 GPa, 61.39 GPa, 32.63 GPa and 0.23, respectively. These findings are consistent with those in Section 3.1.

Table 2. Young's modulus (E), longitudinal modulus (L), bulk modulus (B), shear modulus (G), and Poisson's ratio (υ) of all sintered nanocomposite specimens.

Sample	E	L	B	G	υ
S1	41.20	46.87	29.95	16.92	0.2175
S2	50.21	57.39	36.82	20.57	0.2207
S3	67.23	77.78	50.43	27.35	0.2288
S4	80.55	94.02	61.39	32.63	0.2344

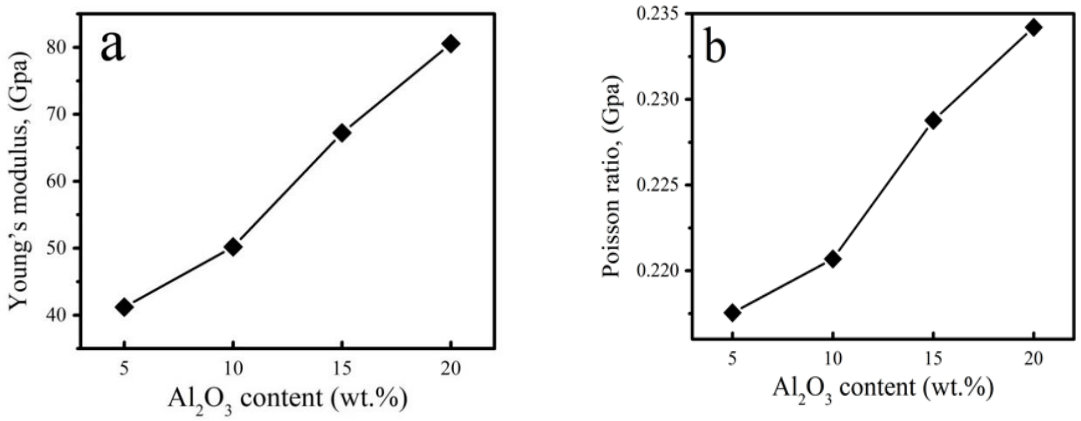

(**a**) (**b**)

Figure 8. (a) Young's modulus (E) and (**b**) Poisson's ratio (ν) of the sintered CHA/Al_2O_3 nanocomposites.

4. Conclusions

This research involved utilizing a high-energy ball mill to create powdered carbonated hydroxyapatite/alumina (CHA/Al_2O_3) nanocomposites with various weight percentages. Powdered nanocomposites were sintered and solidified at a temperature of 1000 °C to test their physical and mechanical characteristics. The following can be used to summarize the most significant results:

- The XRD data showed that when Al_2O_3 contents increased, crystal size decreased.
- Such changes in Al_2O_3 weight% have a demonstrated impact on both lattice strain and dislocation density.
- As the weight fraction of Al_2O_3 rises, the bulk density shows observable increases.
- Decreasing CHA contents adversely impacted porosity.
- There was a noticeable improvement in every mechanical property measured.
- Various biomedical applications can make use of the produced nanocomposites.

Funding

No funding was received.

Acknowledgments

The authors would like to thank the National Research Centre for its support.

Conflicts of Interest

The authors declare no conflict of interest.

References

1. Abushanab, W.S.; Moustafa, E.B.; Youness, R.A. Evaluation of the dynmic behavior, elastic properties, and in vitro bioactivity of some borophosphosilicate glasses for orthopedic applications. *J. Non-Cryst. Solids* **2022**, *586*, 121539, https://doi.org/10.1016/j.jnoncrysol.2022.121539.
2. Youness, R.A.; Amer, M.S; Taha, M.A. Tribo-mechanical measurements and in vivo performance of zirconia-containing biphasic calcium phosphate material implanted in a rat model for bone replacement applications. *Mater. Chem. Phys.* **2022**, *285*, 126085, https://doi.org/10.1016/j.matchemphys.2022.126085.
3. Alturki, A.M.; Abulyazied, D.E.; Taha, M.A.; Abomostafa, H.M.; Youness, R.A. A study to evaluate the bioactivity behavior and electrical properties of hydroxyapatite/Ag_2O-borosilicate glass nanocomposites for biomedical applications. *J. Inorg. Organomet Polym. Mater.* **2022**, *32*, 169-179, https://doi.org/10.1007/s10904-021-02100-3.
4. Youness, R.A.; Taha, M.A. Study of mechanical properties and wear behavior of nano-ZrO_2-hardened Al2024 matrix composites prepared by stir cast method. *Egypt. J. Chem.* **2022**, *65*, 307-313, https://doi.org/10.21608/EJCHEM.2021.85000.4154.
5. AbuShanab, W.S; Moustafa, E.B.; Ghandourah, E., Taha, M.A. Effect of graphene nanoparticles on the physical and mechanical properties of the Al2024-graphene nanocomposites fabricated by powder metallurgy. *Results Phys.* **2020**, *19*, 103343, https://doi.org/10.1016/j.rinp.2020.103343.
6. Bezzina, S.; Moustafa, E.B.; Taha, M.A. Effects of metastable θ' precipitates on the strengthening, wear and electrical behaviors of Al 2519-SiC/fly ash hybrid nanocomposites synthesized by powder metallurgy technique. *Silicon* **2022** In Press, https://doi.org/10.1007/s12633-021-01641-z.
7. Moustafa, E.B.; Mikhaylovskaya, A.V., Taha, M.A.; Mosleh, A.O. Improvement of the microstructure and mechanical properties by hybridizing the surface of AA7075 by hexagonal boron nitride with carbide particles using the FSP process. *J. Mater. Res. Technol.* **2022**, *17*, 1986-1999, https://doi.org/10.1016/j.jmrt.2022.01.150.
8. Moustafa, E.B.; Alazwari, M.A.; Abushanab, W.S; Ghandourah, E.I.; Mosleh, A.O.; Ahmed, H.M.; Taha, M.A. Influence of friction stir process on the physical, microstructural, corrosive, and electrical properties of an Al-Mg alloy modified with Ti-B additives. *Materials* **2022**, *15*, 835, https://doi.org/10.3390/ma15030835.
9. Elkhateeb, W.A.; Morsi, S.S.M.; Hassan, M.E.; Taha, M.A.; Ahmed, E.F; Zaghlol, G.M. Immobilization of Penicillium purpurogenum and application of the produced pigment in plant industry. *Plant Arch.* **2020**, *20*, 857-862.
10. Mohamed, M.A.; Elkhateeb, W.A.; Taha, M.A.; Daba, G.M. New strategies in optimization of Rapamycin production by Streptomyces hygroscopicus ATCC 29253. *Res. J. Pharm. Tech.* **2019**, *12*, 4197-4204, https://doi.org/10.5958/0974-360X.2019.00722.4.
11. Almoselhy, R.I.M.; Eid, M.M.; Abd-Elmageed, S.M.M.; Youness, R.A. Using nanotechnology in bleaching vegetables oils. *Egypt. J. Chem.* **2020**, *63*, 2699-2706, https://doi.org/10.21608/ejchem.2020.23625.2407.
12. Youness, R.A.; Taha, M.A.; Ibrahim, M.A. In vitro bioactivity, molecular structure and mechanical properties of zirconia-carbonated hydroxyapatite nanobiocomposites sintered at different temperatures. *Mater. Chem. Phys.* **2020**, *239*, 122011, https://doi.org/10.1016/j.matchemphys.2019.122011.
13. Taha, M.A.; Youness, R.A.; Zawrah, M.F. Review on nanocomposites fabricated by mechanical alloying. *Int. J. Miner. Metall. Mater.* **2019**, *26*, 1047-1058, https://doi.org/10.1007/s12613-019-1827-4.
14. Sartori, T.A.I.C.; Ferreira, J.A.; Osiro, D.; Colnago, L.A. Pallone, E.M.J.A. Formation of different calcium phosphate phases on the surface of porous Al_2O_3-ZrO_2 nanocomposites. *J. Eur. Ceram. Soc.* **2018**, *38*, 743-751, https://doi.org/10.1016/j.jeurceramsoc.2017.09.014.
15. Abulyazied, D.E; Alturki, A.M.; Youness, R.A. Abomostafa, H.M. Synthesis, structural and biomedical characterization of hydroxyapatite/borosilicate bioactive glass nanocomposites. *J. Inorg. Organomet Polym. Mater.* **2021**, *31*, 4077-4092, https://doi.org/10.1007/s10904-021-02070-6.
16. AbuShanab, W.S.; Moustafa, E.B.; Taha, M.A.; Youness, R.A. Synthesis and structural properties characterization of titania/zirconia/calcium silicate nanocomposites for biomedical applications. *Appl. Phys. A* **2020**, *126*, 787, https://doi.org/10.1007/s00339-020-03975-8.

17. Youness, R.A.; Taha, M.A.; Ibrahim, M. Dense alumina-based carbonated fluorapatite nanobiocomposites for dental applications. *Mater. Chem. Phys.* **2021**, *257*, 123264, https://doi.org/10.1016/j.matchemphys.2020.123264.
18. Taha, M.A.; Youness, R.A; Ibrahim, M. Biocompatibility, physico-chemical and mechanical properties of hydroxyapatite-based silicon dioxide nanocomposites for biomedical applications. *Ceram. Int.* **2020**, *46*, 23599-23610, https://doi.org/10.1016/j.ceramint.2020.06.132.
19. Youness, R.A.; Taha, M.A.; El-Kheshen, A.A. Ibrahim, M. Influence of the addition of carbonated hydroxyapatite and selenium dioxide on mechanical properties and in vitro bioactivity of borosilicate inert glass. *Ceram. Int.* **2018**, *44*, 20677-20685, https://doi.org/10.1016/j.ceramint.2018.08.061.
20. Youness, R.A.; Taha, M.A.; Ibrahim, M.A. Effect of sintering temperatures on the in vitro bioactivity, molecular structure and mechanical properties of titanium/carbonated hydroxyapatite nanobiocomposites. *J. Mol. Struct.* **2017**, *1150*, 188-195, http://dx.doi.org/10.1016/j.molstruc.2017.08.070 .
21. Refaat, A.; Youness, R.A.; Taha, M.A.; Ibrahim, M. Effect of zinc oxide on the electronic properties of carbonated hydroxyapatite. *J. Mol. Struct.* **2017**, *1147*, 148-154, https://doi.org/10.1016/j.molstruc.2017.06.091.
22. Rezakhani, A.; Motlagh, M.M.K. Synthesis and characterization of hydroxyapatite nanocrystal and gelatin doped with Zn^{+} and cross linked by glutaraldehyde. *Int. J. Phys. Sci.* **2012**, *7*, 2768-2774, https://doi.org/10.5897/IJPS11.1676.
23. Youness, R.A.; Taha, M.A.; Ibrahim, M. In vitro bioactivity, physical and mechanical properties of carbonated-fluoroapatite during mechanochemical synthesis. *Ceram. Int.* **2018**, *44*, 21323-21329, https://doi.org/10.1016/j.ceramint.2018.08.184.
24. Youness, R.A.; Taha, M.A.; Ibrahim, M.A. The influence of various zirconia contents on crystallite sizes, shrinkage, and physical and mechanical properties of hydroxyapatite-based nanobiocomposites. *Egypt. J. Chem.* **2021**, *64*, 1347-1352, https://doi.org/10.21608/EJCHEM.2021.38296.2787.
25. Priyadarsini, S.; Mukherjee, S.; Mishra, M. Nanoparticles used in dentistry: A review. *J. Oral Biol. Craniofac. Res.* **2018**, *8*, 58-67, https://doi.org/10.1016/j.jobcr.2017.12.004.
26. Kailasanathan, C.; Selvakumar, N.; Naidu, V. Comparative study of hydroxyapatite/gelatin composites reinforced with bio-inert ceramic particles. *Ceram. Int.* **2012**, *38*, 3569-3582, https://doi.org/10.1016/j.ceramint.2011.12.073.
27. Vahabzadeh, S.; Roy, M.; Bandyopadhyay, A.; Bose, S. Phase stability and biological property evaluation of plasma sprayed hydroxyapatite coatings for orthopedic and dental applications. *Acta Biomater.* **2015**, *17*, 47-55, https://doi.org/10.1016/j.actbio.2015.01.022.
28. Kane, R.J.; Weiss-Bilka, H.E.; Meagher, M.J.; Liu, Y.; Gargac, J.A.; Niebur, G.L.; Wagner, D.R.; Roeder, R.K. Hydroxyapatite reinforced collagen scaffolds with improved architecture and mechanical properties. *Acta Biomater.* **2015**, *17*, 16-25, https://doi.org/10.1016/j.actbio.2015.01.031.
29. Zhou, H.; Lee, J. Nanoscale hydroxyapatite particles for bone tissue engineering. *Acta Biomater.* **2011**, *7*, 2769-2781, https://doi.org/10.1016/j.actbio.2011.03.019.
30. Que, W.; Khor, K.A.; Xu, K.L.; Yu, L.G. Hydroxyapatite/titania nanocomposites derived by combining high-energy ball milling with spark plasma sintering process. *J. Eur. Ceram. Soc.*, **2008**, *28*, 3083-3090, https://doi.org/10.1016/j.jeurceramsoc.2008.05.016.
31. Kuffner, B.H.B.; Facci, A.D.; Sachs, D.; Silva, G. Study of the microstructure and mechanical properties of beta tricalcium phosphate-based composites with alumina addition produced by powder metallurgy. *Int. Eng. J. Ouro Petro* **2017**, *70*, 459-464, http://dx.doi.org/10.1590/0370-44672017700082.
32. Vijayalakshmi, V.; Dhanasekaran, P. Synthesis and structural properties characterization of HA/alumina and HA/MgO nanocomposite for biomedical applications. *Trans. Med. Res.* **2018**, *7*, 1238-1247, https://doi.org/10.20959/wjpr20181-7562.
33. Guidara, A.; Chaari, K.; Bouaziz, J. Elaboration and characterization of alumina-fluorapatite composites. *J. Biomater. Nanobiotechnol.* **2011**, *2*, 103-113, https://doi.org/10.4236/jbnb.2011.22014.
34. Family, R.; Solati-Hashjin, M.; Nik, S.N.; Nemati, A. Surface modification for titanium implants by hydroxyapatite nanocomposite. *Caspian J. Intern Med.* **2012**, *3*, 460-465.
35. Youness, R.A.; Taha, M.A.; Elhaes, H.; Ibrahim, M. Molecular modeling, FTIR spectral characterization and mechanical properties of carbonated-hydroxyapatite prepared by mechanochemical synthesis. *Mater. Chem. Phys.* **2017**, *190*, 209-218,http://dx.doi.org/10.1016/j.matchemphys.2017.01.004.

36. Youness, R.A.; Taha, M.A.; Elhaes, H.; Ibrahim, M. Preparation, Fourier transform infrared characterization and mechanical properties of hydroxyapatite nanopowders. *J. Comput. Theor. Nanosci.* **2017**, *14*, 2409-2415, http://dx.doi.org/10.1166/jctn.2017.6841.
37. Khattab, R.M.; Sadek, H.E.H.; Taha, M.A.; El-Rafei, A.M. Recycling of silica fume waste in the manufacture of β-eucryptite ceramics. *Mater. Character.* **2021**, *171*, 110740, https://doi.org/10.1016/j.matchar.2020.110740.
38. Hessien, M.A.; Khattab, R.M.; Taha, M.A.; Sadek, H.E.H. Fabrication of porous Al2O3-MgO-TiO2 ceramic monoliths by the combination of nanoemulsion templating and temperature-induced forming. *J. Eur. Ceram. Soc.* **2021**, *41*, 1514-1523, https://doi.org/10.1016/j.jeurceramsoc.2020.09.056.
39. Youness, R.A.; Taha, M.A.; El-Kheshen, A.A.; El-Faramawy, N.; Ibrahim, M. In vitro bioactivity evaluation, antimicrobial behavior and mechanical properties of cerium-containing phosphate glasses. *Mater. Res. Express* **2019**, *6*, 075212, https://doi.org/10.1088/2053-1591/ab15b5.
40. Youness, R.A.; Ibrahim, M.; Taha, M.A. Evaluation of the electrical and dielectric behavior of the apatite layer formed on the surface of hydroxyapatite/hardystonite/copper oxide hybrid nanocomposites for bone repair applications. *Ceram. Int.* **2022**, *48*, 19837-19850, https://doi.org/10.1016/j.ceramint.2022.03.259.
41. Khalil, E.M.A.; Youness, R.A.; Amer, M.S.; Taha, M.A. Mechanical properties, in vitro and in vivo bioactivity assessment of Na_2O-CaO-B_2O_3-SiO_2 glass-ceramics. *Ceram. Int.* **2018**, *44*, 7867-7876, https://doi.org/10.1016/j.ceramint.2018.01.222.
42. Taha, M.A.; Youness, R.A.; El-Bassyouni, G.T.; Azooz, M.A. FTIR spectral characterization, mechanical and electrical properties of P_2O_5-Li_2O-CuO glass-ceramics. *Silicon* **2021**, *13*, 3075-3084, https://doi.org/10.1007/s12633-020-00661-5.
43. Alatawi, A.S.; Alturki, A.M.; Soliman, G.M.; Abulyazied, D.E.; Taha, M.A.; Youness, R.A. Improved toughness, electrical conductivity and optical properties of bioactive borosilicate glasses for orthopedic applications. *Appl. Phys. A* **2021**, *127*, 971, https://doi.org/10.1007/s00339-021-05116-1.
44. AbuShanab, W.S.; Moustafa, E.B.; Ghandourah, E.; Taha, M.A. Effect of graphene nanoparticles on the physical and mechanical properties of the Al2024-graphene nanocomposites fabricated by powder metallurgy. *Results Phys.* **2020**, *19*, 103343, https://doi.org/10.1016/j.rinp.2020.103343.
45. Moustafa, E.B.; Taha, M.A. Preparation of high strength graphene reinforced Cu-based nanocomposites via mechanical alloying method: microstructural, mechanical and electrical properties. *Appl. Phys. A* **2020,** *126*, 220, https://doi.org/10.1007/s00339-020-3412-0.
46. Zawrah, M.F.; El-Meligy, W.M.; Saudi, H.H.A.; Ramadan, S.; Taha, M.A. Mechanical and electrical properties of nano Al-Matrix composites reinforced with SiC and prepared by powder metallurgy. Biointerface *Res. Appl. Chem.* **2022**, *12*, 2068-2083, https://doi.org/10.33263/BRIAC122.20682083.
47. Moustafa, E.B.; Taha, M.A. Evaluation of the microstructure, thermal and mechanical properties of Cu/SiC nanocomposites fabricated by mechanical alloying. *Int. J. Miner. Metall. Mater.* **2021**, *28*, 475-486, https://doi.org/10.1007/s12613-020-2176-z.
48. Laasri, S.; Taha, M.; Hlil, E.K.; Laghzizil, A.; Hajiaji. Manufacturing and mechanical properties of calcium phosphate biomaterials. *C.R. Mecanique* **2012**, *340*, 715-720, https://doi.org/10.1016/j.crme.2012.09.005.
49. Hannora, A.E.; Ataya, S. Structure and compression strength of hydroxyapatite/titania nanocomposites formed by high energy ball milling. *J. Alloys Compd.* **2016**, *658*, 222-233, http://dx.doi.org/10.1016/j.jallcom.2015.10.240.
50. Mahmoodi, M.; Hashemi, P.M.; Imani, R. Characterization of a novel nanobiomaterials fabricated from HA, TiO_2 and Al_2O_3 powders: an in vitro study. *Prog. Biomater.* **2014**, *3*, 25, https://doi.org/10.1007/s40204-014-0025-8.
51. Prakasam, M.; Locs, J.; Salma-Ancane, K.; Loca, D.; Largeteau, A.; Berzina-Cimdina, L. Fabrication, properties and applications of dense hydroxyapatite: a review. *J. Funct. Biomater.* **2015**, *6*, 1099-1140, https://doi.org/10.3390/jfb6041099.
52. Encinas-Romero, M.A.; Peralta-Haley, J.; Valenzuela-Garcia, J.L.; Castillon-Barrza, F.F. Synthesis and structural characterization of hydroxyapatite-wollastonite biocomposites, produced by an alternative sol-gel route. *J. Biomater. Nanotechnol.* **2013**, *4*, 327-333, http://dx.doi.org/10.4236/jbnb.2013.44041.
53. Rahaman, M.N.; Day, D.E.; Bal, B.S.; Fu, Q.; Jung, S.B.; Bonewald, L.F.; Tomsia, A.P. Bioactive glass in tissue engineering. *Acta Biomater.* **2011**, *7*, 2355-2373, https://doi.org/10.1016/j.actbio.2011.03.016.